AIAA JOURNAL
Vol. 41, No. 8, August 2003

Large-Eddy Simulation of Supersonic Cavity Flowfields Including Flow Control

Donald P. Rizzetta* and Miguel R. Visbal†
U.S. Air Force Research Laboratory, Wright–Patterson Air Force Base, Ohio 45433-7512

Large-eddy simulations of supersonic cavity flowfields are performed using a high-order numerical method. Spatial derivatives are represented by a fourth-order compact approximation that is used in conjunction with a sixth-order nondispersive filter. The scheme employs a time-implicit approximately factored finite difference algorithm, and applies Newton-like subiterations to achieve second-order temporal and fourth-order spatial accuracy. The Smagorinsky dynamic subgrid-scale model is incorporated in the simulations to account for the spatially underresolved stresses. Computations at a freestream Mach number of 1.19 are carried out for a rectangular cavity having a length-to-depth ratio of 5:1. The computational domain is described by 2.06×10^7 grid points and has been partitioned into 254 zones, which were distributed on individual processors of a massively parallel computing platform. Active flow control is applied through pulsed mass injection at a very high frequency, thereby suppressing resonant acoustic oscillatory modes. Features of the flowfields are elucidated, and comparisons are made between the unsuppressed and suppressed cases and with available experimental data that were collected at a higher Reynolds number.

Nomenclature

C_p	=	time–mean pressure coefficient
d	=	dimensional cavity depth
E_{k_z}	=	turbulence kinetic energy spanwise wave number spectra
E_ω	=	turbulent kinetic energy frequency spectra
$\boldsymbol{F}, \boldsymbol{G}, \boldsymbol{H}$	=	inviscid vector fluxes
$\boldsymbol{F}_v, \boldsymbol{G}_v, \boldsymbol{H}_v$	=	viscous vector fluxes
j	=	dimensional mass-injection slot width
K	=	turbulent kinetic energy
k_z	=	nondimensional spanwise wave number
l	=	dimensional cavity length
p	=	nondimensional static pressure
$\boldsymbol{Q}$	=	vector of dependent variables
Re	=	reference Reynolds number, $\rho_\infty u_\infty l/\mu_\infty$
Re_δ	=	boundary-layer thickness Reynolds number
Re_θ	=	momentum thickness Reynolds number
S	=	dimensional spanwise domain extent
T	=	nondimensional static temperature
t	=	nondimensional time
u, v, w	=	nondimensional Cartesian velocity components in x, y, and z directions
x, y, z	=	nondimensional Cartesian coordinates in the streamwise, vertical, and spanwise directions
x_u, x_d	=	dimensional streamwise exterior cavity extents
y_t	=	dimensional vertical domain extent
$\Delta\boldsymbol{Q}$	=	$\boldsymbol{Q}^{p+1} - \boldsymbol{Q}^p$
Δt	=	time step size
$\Delta x, \Delta y, \Delta z$	=	mesh step sizes
δ	=	dimensional boundary-layer thickness
$\delta_{\xi 2}, \delta_{\eta 2}, \delta_{\zeta 2}, \delta_{\xi 4}, \delta_{\eta 4}, \delta_{\zeta 4}$	=	second-order and fourth-order finite difference operators in ξ, η, and ζ directions
ξ, η, ζ	=	computational coordinates
ρ	=	nondimensional fluid density
ω	=	frequency, Hz

Subscripts

m	=	time-mean value
0	=	evaluated at the inflow location
∞	=	freestream value

Superscripts

n	=	time level
p	=	subiteration level
$\sim$	=	Favre-averaged component
$\breve{}$	=	numerically filtered value
$'$	=	fluctuating component
$+$	=	value given in law-of-the-wall units

Introduction

HIGH-SPEED flows over open cavities produce complex unsteady interactions, which are characterized by a severe acoustic environment. At high Reynolds numbers, such flowfields comprised both broadband small-scale fluctuations typical of turbulent shear layers and discrete resonance, whose frequency and amplitude depend on the cavity geometry and external flow conditions. Although these phenomena are of fundamental physical interest, they also represent a number of significant concerns for aerospace applications. In the practical situation of an aircraft weapons bay, aerodynamic performance or stability may be adversely affected, structural loading may become excessive, and sensitive instrumentation may be damaged. Acoustic resonance can also pose a threat to the safe release and accurate delivery of weapons systems stored within the cavity.

Because of the intricate nature and practical significance of supersonic cavity flows, numerous experimental investigations[1–14] have been conducted to understand their underlying physical behavior. For the present investigation, we consider a deep cavity where the length-to-depth ratio is less than 9. In this situation, the boundary layer ahead of the upstream lip forms into a free shear layer, which then flows over the cavity and impinges upon the rear bulkhead. The undulating shear layer generates strong compression waves both external and internal to the cavity and results in periodic addition or removal of mass from the cavity at the downstream bulkhead, thereby, producing a self-sustained fluid oscillation. A more complete

Presented as Paper 2002-2853 at the AIAA 32nd Fluid Dynamics Conference, St. Louis, MO, 24–26 June 2002; received 28 June 2002; revision received 22 January 2003; accepted for publication 21 March 2003.

*Senior Research Aerospace Engineer, Computational Sciences Branch, Aeronautical Sciences Division. Associate Fellow AIAA.

†Technical Area Leader, Computational Sciences Branch, Aeronautical Sciences Division. Associate Fellow AIAA.

description of the oscillation cycle and corresponding wave system structure may be found in Refs. 10 and 15.

A simplified rational model developed by Rossiter[5] has proven to be successful for describing the realizable set of cavity resonant frequencies. It is based on a feedback loop whereby the undulating shear layer is considered to consist of a series of vortices that originate at the upstream cavity lip and travel downstream at a uniform velocity. On reaching the downstream lip, the vortices immediately give rise to upstream moving acoustic waves that propagate at the local speed of sound. When these waves impact the upstream lip, they trigger the production of new vortices, thus, completing the feedback cycle. From this basic concept, Rossiter then constructed an empirical expression defining the potential fluctuation frequencies.

Although Rossiter's formula identifies the probable modes of supersonic cavity oscillations, it cannot predict which of these modes will actually be excited. Moreover, no simple relationship exists for obtaining amplitudes of the associated pressure fluctuations within the cavity. Numerical solutions of the governing fluid equations of motion have been utilized to provide this and other detailed information of both mean and instantaneous flowfields.[14–22] Whereas the majority of these calculations have been two dimensional,[16–20] some three-dimensional computations have also been carried out.[14,15,21,22] In all cases, the Reynolds-averaged Navier–Stokes (RANS) equations were considered, and various models were utilized to account for the effects of turbulence, indirectly. More recently, large-eddy simulation (LES)[23] and hybrid (RANS/LES)[24] methods have been employed to describe some elements of high-Reynolds-number cavity flowfields. In these computations, small-scale fluid structures of the upstream turbulent boundary layer were not characterized.

Because of the aforementioned undesirable attributes of cavity resonance, many classic mechanisms have been devised for its suppression.[9,13] These include modification of the downstream cavity geometry to mitigate mass addition and removal, steady cross-stream fluid injection upstream of the cavity, and the use of leading-edge spoilers. The latter two of these methods generate a large-scale disruption of the shear layer that precludes its impingement upon the rear bulkhead. Although each system was able to achieve some reduction in sound pressure levels of resonant acoustic modes, penalties were incurred with regard to increased drag, additional mechanical complexity, or excessive injected mass flow rate.

Active flow control has been proposed as a means of reducing acoustic levels in aircraft weapons bays over a wide range of flight conditions.[25] Under this procedure, suppression is achieved by perturbing the unstable shear layer through pulsed mass injection. Attempts to attain control by forcing at frequencies near the dominant Rossiter modes have met with limited success.[25,26] It has been shown, however, that perturbations introduced at very high frequencies can lead to active suppression of multiple acoustic resonant modes.[27]

The objective of the present effort is to perform LES of the turbulent supersonic flow past an open rectangular cavity. In particular, small-scale fluid structures in the upstream boundary layer approaching the cavity are accounted for as part of the computation. Additionally, high-frequency forcing, via pulsed mass injection upstream of the forward cavity lip, was considered numerically to investigate the ability of LES to predict acoustic resonance suppression. For both unsuppressed and suppressed cases, experimental data are available for comparative purposes in the form of instantaneous pressure measurements[27–30] on interior cavity surfaces.

The cavity geometric configuration is represented schematically in Fig. 1, where the length to depth ratio $l/d = 5.0$ and the freestream

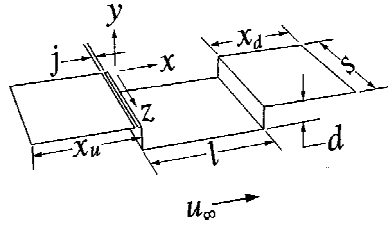

Fig. 1 Cavity configuration schematic.

Table 1 Cavity flow conditions

Method	Re	$Re_{\delta 0}$	$Re_{\theta 0}$
Present LES	2.00×10^5	6.774×10^3	667
Experiment[27–30]	3.01×10^6	5.17×10^4	5.03×10^3

Mach number is 1.19. Conditions at which experimental measurements were taken[27–30] correspond to a Reynolds number of 3.01×10^6 based on the cavity length l. Because it would not be possible to numerically resolve fine-scale turbulent structures at the experimental Reynolds number, simulations were carried out for $Re = 2.0 \times 10^5$. Reference quantities in terms of the incoming boundary-layer parameters are provided in Table 1.

Governing Equations

The governing equations are the unsteady three-dimensional compressible Favre filtered Navier–Stokes equations, written in non-dimensional variables and expressed notationally in the following conservative form:

$$\frac{\partial \boldsymbol{Q}}{\partial t} + \frac{\partial}{\partial \xi}\left(\boldsymbol{F} - \frac{1}{Re}\boldsymbol{F}_v\right) + \frac{\partial}{\partial \eta}\left(\boldsymbol{G} - \frac{1}{Re}\boldsymbol{G}_v\right) \frac{\partial}{\partial \zeta}\left(\boldsymbol{H} - \frac{1}{Re}\boldsymbol{H}_v\right) = 0 \tag{1}$$

where t is the time. A more detailed set of these equations may be found in Refs. 31 and 32 and is not reproduced here.

Spatially underresolved stresses in the LES are represented by the Smagorinsky dynamic subgrid-scale model, which was first proposed by Germano et al.[33] for for incompressible flows. The present computations incorporate Yoshizawa's[34] treatment of the stress tensor and extensions of the dynamic model by Moin et al.[35] for compressible applications. A comprehensive development of the model equations appears in Refs. 31 and 32.

Numerical Method

Time-accurate solutions to Eq. (1) were obtained numerically by the implicit approximately factored finite difference algorithm of Beam and Warming[36] employing Newton-like subiterations (see Ref. 37), which has evolved as an efficient tool for generating solutions to a wide variety of complex fluid flow problems and may be represented notationally as follows:

$$\begin{aligned}
&\left[I + \left(\frac{2\Delta t}{3}\right)\delta_{\xi 2}\left(\frac{\partial \boldsymbol{F}^p}{\partial \boldsymbol{Q}} - \frac{1}{Re}\frac{\partial \boldsymbol{F}_v^p}{\partial \boldsymbol{Q}}\right)\right] \\
&\quad \times \left[I + \left(\frac{2\Delta t}{3}\right)\delta_{\eta 2}\left(\frac{\partial \boldsymbol{G}^p}{\partial \boldsymbol{Q}} - \frac{1}{Re}\frac{\partial \boldsymbol{G}_v^p}{\partial \boldsymbol{Q}}\right)\right] \\
&\quad \times \left[I + \left(\frac{2\Delta t}{3}\right)\delta_{\zeta 2}\left(\frac{\partial \boldsymbol{H}^p}{\partial \boldsymbol{Q}} - \frac{1}{Re}\frac{\partial \boldsymbol{H}_v^p}{\partial \boldsymbol{Q}}\right)\right]\Delta \boldsymbol{Q} \\
&\quad = -\left(\frac{2\Delta t}{3}\right)\left[\left(\frac{1}{2\Delta t}\right)(3\boldsymbol{Q}^p - 4\boldsymbol{Q}^n + \boldsymbol{Q}^{n-1}) \right. \\
&\quad + \delta_{\xi 4}\left(\boldsymbol{F}^p - \frac{1}{Re}\boldsymbol{F}_v^p\right) + \delta_{\eta 4}\left(\boldsymbol{G}^p - \frac{1}{Re}\boldsymbol{G}_v^p\right) \\
&\quad \left. + \delta_{\zeta 4}\left(\boldsymbol{H}^p - \frac{1}{Re}\boldsymbol{H}_v^p\right)\right]
\end{aligned} \tag{2}$$

In this expression, which was employed to advance the solution in time, $\boldsymbol{Q}^{p+1}$ is the $p+1$ approximation to $\boldsymbol{Q}$ at the $n+1$ time level $\boldsymbol{Q}^{n+1}$, and $\Delta \boldsymbol{Q} = \boldsymbol{Q}^{p+1} - \boldsymbol{Q}^p$. For $p = 1$, $\boldsymbol{Q}^p = \boldsymbol{Q}^n$. Second-order-accurate backward-implicit time differencing has been used to represent temporal derivatives.

The implicit segment of the algorithm incorporated second-order-accurate centered differencing for all spatial derivatives and utilized nonlinear artificial dissipation[38] to augment stability. Efficiency was enhanced by solving this implicit portion of the factorized equations

in diagonalized form.[39] Temporal accuracy, which can be degraded by use of the diagonal form, is maintained by utilizing subiterations within a time step. This technique has been commonly invoked to reduce errors due to factorization, linearization, and explicit application of boundary conditions. It is useful for achieving temporal accuracy on overset zonal mesh systems and for a domain decomposition implementation on parallel computing platforms. As the subiteration process proceeds, $\Delta \boldsymbol{Q} \longrightarrow 0$. Thus, any deterioration of the solution incurred by use of artificial dissipation and lower-order spatial difference operators on the right-hand side of Eq. (2) is reduced by the procedure. Three subiterations per time step have been applied for the computations presented here.

The compact difference scheme employed on the right-hand side of Eq. (2) is based on the pentadiagonal system of Lele[40] and is capable of attaining spectrallike resolution. This is achieved through the use of a centered implicit difference operator with a compact stencil, thereby, reducing the associated discretization error. The fourth-order tridiagonal subset of Lele's system is illustrated here in one spatial dimension as

$$\alpha\left(\frac{\partial \boldsymbol{F}}{\partial \xi}\right)_{i-1} + \left(\frac{\partial \boldsymbol{F}}{\partial \xi}\right)_{i} + \alpha\left(\frac{\partial \boldsymbol{F}}{\partial \xi}\right)_{i+1} = a\left(\frac{\boldsymbol{F}_{i+1} - \boldsymbol{F}_{i-1}}{2}\right) \quad (3)$$

with $\alpha = \frac{1}{4}$ and $a = \frac{3}{2}$. The scheme has been adapted by Visbal and Gaitonde[41] as an implicit iterative time-marching technique, applicable for unsteady vortical flows. It is used in conjunction with a sixth-order nondispersive spatial filter developed by Gaitonde et al.,[42] which has been shown to be superior to the use of explicitly added low-order, scalar artificial dissipation for maintaining both stability and accuracy on stretched curvilinear meshes.[41] The filter is applied to the solution vector sequentially in each of the three computational directions following each subiteration and is implemented as

$$\alpha_f \check{\boldsymbol{Q}}_{i-1} + \check{\boldsymbol{Q}}_i + \alpha_f \check{\boldsymbol{Q}}_{i+1} = \sum_{n=0}^{3} \frac{a_n}{2}(\boldsymbol{Q}_{i+n} + \boldsymbol{Q}_{i-n}) \quad (4)$$

where $\check{\boldsymbol{Q}}$ is the filtered value of $\boldsymbol{Q}$. Equation (4) represents a one-parameter family of filters, where numerical values for α_f and the a_n may be found in Ref. 43.

The aforementioned features of the numerical algorithm are embodied in a parallel version of the time-accurate three-dimensional computer code FDL3DI,[43] which has proven to be reliable for steady and unsteady fluid flow problems, including the simulation of flows over delta wings with leading-edge vortices,[44–47] vortex breakdown,[45–47] direct numerical simulation (DNS) of transitional wall jets[48] and synthetic jet actuators,[49] and DNS and LES of subsonic[50] and supersonic flowfields.[32,51]

Computational Mesh

The computational domain surrounding the cavity flowfield was described by a nonuniform Cartesian mesh, whose origin was located at the upstream inboard cavity lip (Fig. 1). Geometrical extents indicated in Fig. 1 had the following values:

$$x_u/l = 0.83, \qquad x_d/l = 0.80, \qquad S/l = 0.10 \quad (5)$$

A mass-ejection slot for active flow control had a width of

$$j/l = 0.025 \quad (6)$$

which is the same as that of the experimental configuration.[27–30] The upper boundary of the domain y_t was located at $2.0l$. In terms of the time–mean incoming boundary-layer thickness δ_0, the extents indicated in Fig. 1 correspond to

$$x_u = 24.4\delta_0, \qquad l = 29.5\delta_0, \qquad x_d = 23.6\delta_0 \quad (7)$$

Additionally,

$$d = 5.9\delta_0, \qquad y_t = 59.0\delta_0, \qquad S = 3.0\delta_0 \quad (8)$$

Grid points were apportioned in the x direction as

$$N_{x_u} = 270, \qquad N_l = 350, \qquad N_{x_d} = 105, \qquad N_j = 40 \quad (9)$$

whereas the vertical and spanwise distributions employed the following:

$$N_d = 121, \qquad N_{y_t} = 221, \qquad N_S = 101 \quad (10)$$

This resulted in a computational mesh size of $725 \times 221 \times 101$ grid points for the region exterior to the cavity and $351 \times 121 \times 101$ points within the cavity itself. For the lower domain, four $x-z$ planes of grid points extend above $y = 0.0$ and were overset into the upper portion of the flowfield. All of these points, including those at $y = 0.0$, were coincident between the two regions. Minimum mesh spacings occurred at the cavity corners in the x direction and along $y = 0$ vertically. A constant spacing was utilized spanwise. Most of the grid points exterior to the cavity were concentrated vertically in $0.0 \le y \le 0.2$.

Streamwise mesh spacings in wall units had the following values. At the upstream boundary,

$$\Delta x^+ = 31.6 \quad (11)$$

at the cavity lips,

$$\Delta x^+ = 6.4 \quad (12)$$

and at $x = 0.5$,

$$\Delta x^+ = 33.1 \quad (13)$$

The vertical spacing at $y = 0.0$ was

$$\Delta y^+ = 1.6 \quad (14)$$

and a uniform z distribution resulted in

$$\Delta z^+ = 7.5 \quad (15)$$

Grid lines in the x direction were rapidly stretched from $x = 1.2$ to the downstream boundary at $x = 1.8$. This rapid stretching, in conjunction with the numerical filter, was used to provide a nonreflective buffer zone. Geometric stretching of y grid lines was employed for $0.0 \le y \le 0.2$, with a constant spacing ratio of 1.013. Beyond $y = 0.2$, rapid stretching to the upper domain boundary was again enforced. At spanwise domain boundaries, an overlap of five $x-y$ grid planes in the z direction was employed to facilitate application of periodic conditions.

Inflow Profiles

Inflow data for the cavity flowfields were obtained from a spatially evolving flat plate simulation, which was used to produce profiles of the dependent variables. This procedure is essentially identical to that used previously for supersonic compression-ramp computations[32,51] and is briefly summarized here. The flat plate computational domain consisted of a constant streamwise mesh spacing [Eq. (11)] and a grid structure in the $y-z$ plane that was identical to that of the exterior cavity flowfield. A compressible Blasius solution was used to initialize all dependent variables on a mesh consisting of $301 \times 221 \times 101$ points. Variables were perturbed at the upstream boundary, resulting in transition just downstream, and the solution was allowed to develop temporally sufficiently long so that statistically meaningful data could be obtained. No subgrid-stress model was employed in the computation.

From the time–mean flowfield, a streamwise location was determined where profile information was to be extracted as inflow data for the cavity simulations. At the selected position, the mean boundary layer had the thickness $\delta_0/l = 0.03387$. This was intentionally taken to be approximately twice that of the experimental value to allow satisfactory spatial resolution. For the resulting profile, 87 grid points in the vertical direction were within the boundary layer.

The flat plate simulation then continued to evolve for 5100 time steps, during which all dependent variables at each grid point in the specified $y-z$ plane were recorded. These data were made periodic in time by averaging the first 100 and last 100 planes of

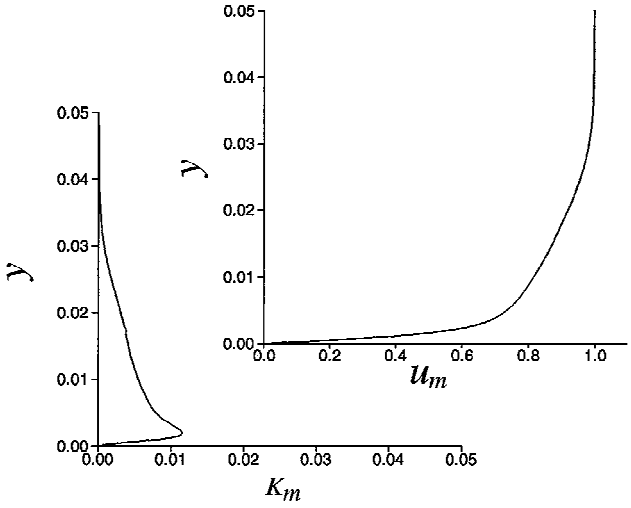

Fig. 2 Spanwise-averaged time–mean streamwise velocity and turbulent kinetic energy profiles for the cavity domain inflow.

information, to obtain a set of 5000 profiles. The nondimensional time period of these data corresponds to $t = 71.9\delta_0/l$. When the data were made periodic, they could then be recycled into the cavity flowfield for computational times greater then $t = 71.9\delta_0/l$, thereby reducing computational expense. Moreover, the period is adequate to avoid artificial forcing of the boundary layer at a frequency below its characteristic value and ensures that the inflow data are decorrelated before they are recycled.[52] Because the vertical and spanwise grids for the flat plate and cavity inflow domains are identical, no spatial interpolation of the data was required. Spanwise-averaged time–mean streamwise velocity and turbulent kinetic energy profiles are shown in Fig. 2, which are seen to be characteristic of a flat plate boundary layer.

Details of the Computations

For all simulations, including those used to generate inflow data, the time step was specified as $\Delta t = 4.87 \times 10^{-4}$. This represents a value of

$$\Delta t^+ = 0.27 \tag{16}$$

in wall units and was chosen to provide 300 time steps over one period of the forced mass injection frequency of 5000 Hz. Some preliminary unsteady two-dimensional RANS computations were performed, and an instantaneous result was distributed uniformly in the spanwise direction to initialize the three-dimensional flowfield. The unsuppressed case was then allowed to develop temporally for 30,000 time steps. This duration was required for the fine-scale structures, contained in the inflow profiles, to influence the unsteady solution and for the initial two-dimensional features to evolve to a fully three-dimensional state. Processing of the solution then continued for an additional 50,000 time steps, over which statistical information was recorded. The flowfield for the suppressed case was initialized from the unsuppressed simulation, allowed to develop for 4500 time steps, and then processed for 50,000 steps.

At the inflow boundary, instantaneous values obtained by the aforementioned procedure were prescribed for all dependent variables. Simple extrapolation was employed at the outflow plane downstream of the stretched-mesh region. On all solid surfaces, the no-slip condition was enforced together with a fourth-order-accurate representation of zero normal pressure gradient. The isothermal temperature $T = 1.25$ was also specified on these surfaces, which corresponds to the adiabatic wall value. Because the freestream flow was supersonic, simple extrapolation was applied along the upper boundary. At the spanwise ends of the domain, periodicity was implemented using the overlapping grid planes.

Active flow control, applied to produce suppression of resonant acoustic oscillatory modes within the cavity, was simulated by specifying a velocity profile exiting through the mass-ejection slot

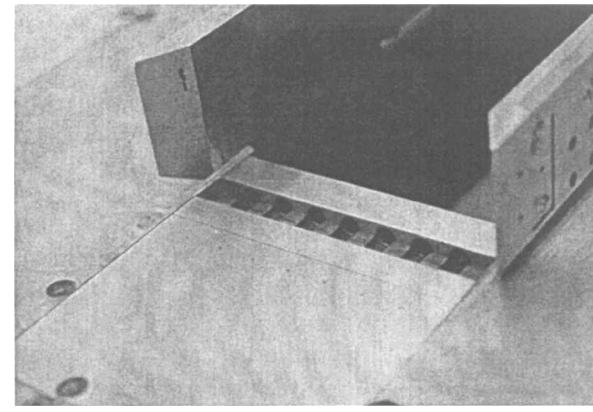

Fig. 3 Experimental cavity configuration.

shown in Fig. 1. This profile had the following assumed functional description:

$$v = A \sin(\omega_x) \sin^2(0.5\omega_t t) \tag{17}$$

$$\omega_x = \pi \left(\frac{x - x_{j1}}{x_{j2} - x_{j1}} \right) \tag{18}$$

$$\omega_t = \frac{2\pi l \times 5000}{u_\infty} \tag{19}$$

In the preceding equations, x_{j1} and x_{j2} are the upstream and downstream extents of the slot, respectively, and A is an amplitude that could be adjusted to control the mass-flow rate. The assumed profile generates a fluctuating injection velocity that is always positive. At the plane of the jet exit, the pressure was obtained from the inviscid normal momentum equation, and the jet was assumed to be isothermal at the wall temperature.

Several differences exist between the computed flowfields and the experimental configuration that they attempt to simulate, which is shown in Fig. 3. Figure 3 shows sidewall surfaces that mimic weapons bay doors in the open position. The width-to-length ratio of the configuration is 0.2, which is about twice that of the computational domain. Mass injection is delivered by a series powered resonance tubes[27,53] located beneath the jet exit. These tubes are fed by a single plenum and discharge through the common slot. The expelled flow is probably neither two dimensional nor isothermal, but the complex nature of the interior region below the slot is beyond the scope of the present work.

The two-block computational mesh described earlier was decomposed into 254 separate domains, each of which was distributed on an individual processor of a massively parallel computing platform (IBM SP3). This decomposition was constructed to provide an approximately equal number of grid points in each domain, thereby balancing the computational work load among the processors. Faces at the boundaries of each block were overset into adjacent domains, such that an overlap of five planes was established. Although this incurred an overhead due to redundant computation, it maintained both the high-order difference and numerical filtering schemes. Because all overlapping mesh points were coincident, no interpolation was required. Automated software[54] was used to identify donor and recipient points, and internode communication among the processors was established through standard message-passing interface library routines.[55]

Results

In the results that follow, large-scale variables were decomposed into time–mean values and fluctuating components, for example,

$$\tilde{u} = u_m + u' \tag{20}$$

Time–Mean Flowfields

Features of the time–mean cavity flowfields are shown in Figs. 4–11. For all of these results, information was obtained by

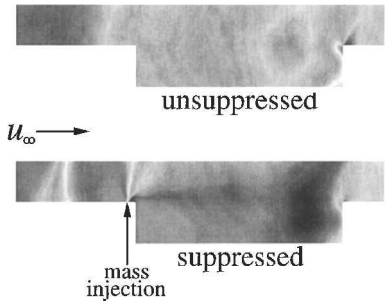

Fig. 4 Spanwise-averaged time–mean pressure coefficient contours.

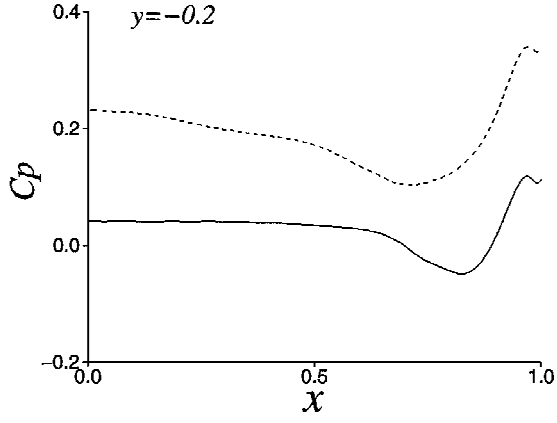

Fig. 5 Spanwise-averaged time–mean pressure coefficient distributions on the cavity floor: - - - -, unsuppressed and ——, suppressed.

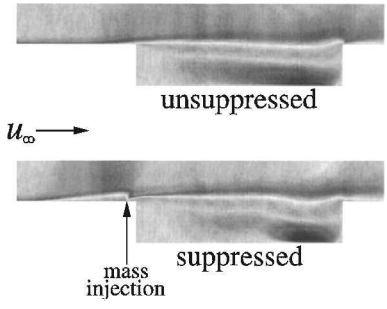

Fig. 6 Spanwise-averaged time–mean steamwise velocity contours.

spatial averaging in the homogeneous direction (spanwise), as well as temporally. Figure 4 shows contours of the mean pressure coefficient. Dark areas represent regions of low pressure, whereas high pressures are lighter. A weak oblique shock lies a distance of approximately one cavity depth upstream of the forward bulkhead in the unsuppressed case and more than twice that distance when mass injection is active. Pressure levels within the cavity are noticeably lower (darker) in the suppressed case. A low-pressure region at the mouth of the cavity upstream of the aft bulkhead is seen in the unsuppressed case. For the suppressed case, the pressure in this area is lower, and its vertical extent is much greater. A more quantitative comparison of the mean pressure levels is provided by the distributions along the cavity floor ($y = -0.2$) in Fig. 5. Reduction in the level of Cp due to suppression is apparent.

Time–mean streamwise velocity contours appear in Fig. 6. A thickening of the boundary layer upstream of mass injection can be observed in the suppressed case. Also noted in the suppressed case is a reduction in size of the low-speed region within the cavity near the rear bulkhead. Profiles of the mean streamwise velocity at three locations are shown in Fig. 7. A reduction in reversed flow for the suppressed case at $x = 0.5$ is evident.

Contours of mean turbulent kinetic energy are found in Fig. 8. Although the level of the kinetic energy is elevated in the immediate vicinity of the injection slot due to high-frequency forcing, its

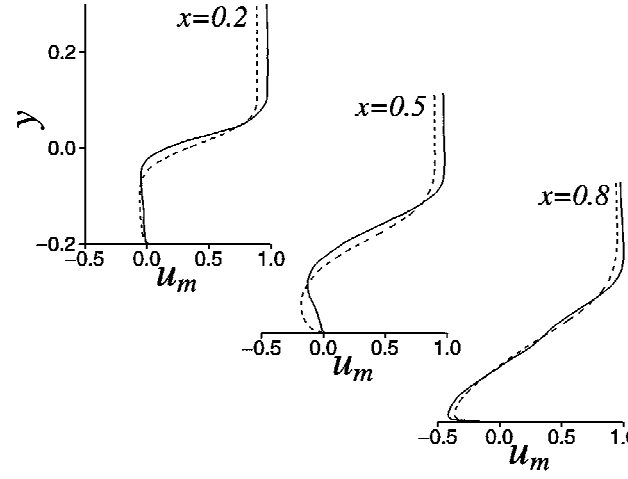

Fig. 7 Spanwise-averaged time–mean steamwise velocity profiles: - - - -, unsuppressed and ——, suppressed.

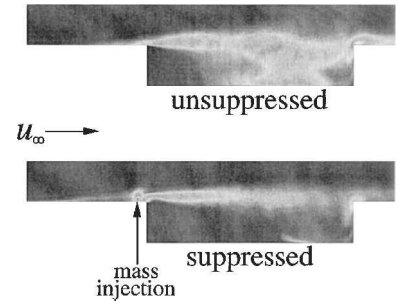

Fig. 8 Spanwise-averaged time–mean turbulent kinetic energy contours.

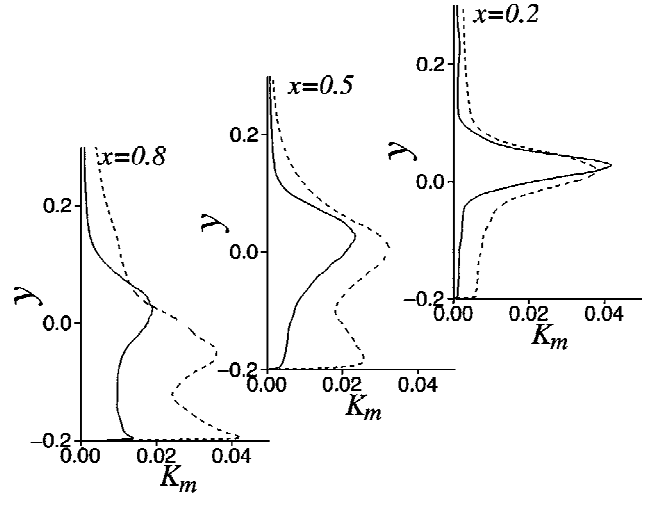

Fig. 9 Spanwise-averaged time–mean turbulent kinetic energy profiles: - - - -, unsuppressed and ——, suppressed.

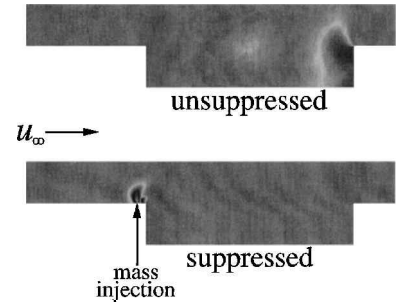

Fig. 10 Spanwise-averaged time–mean fluctuating pressure contours.

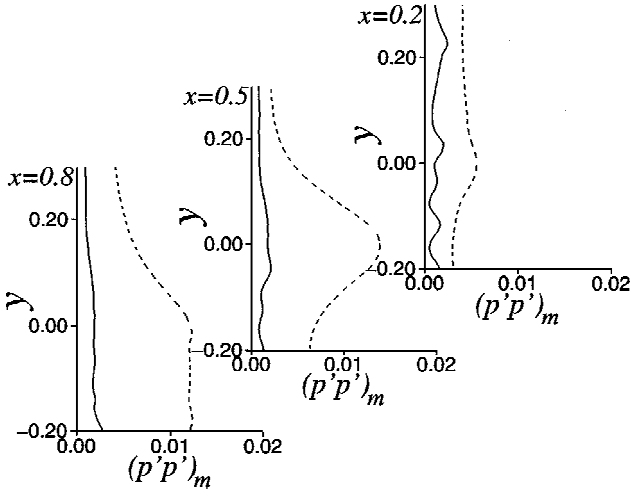

Fig. 11 Spanwise-averaged time–mean fluctuating pressure profiles: - - - -, unsuppressed and ——, suppressed.

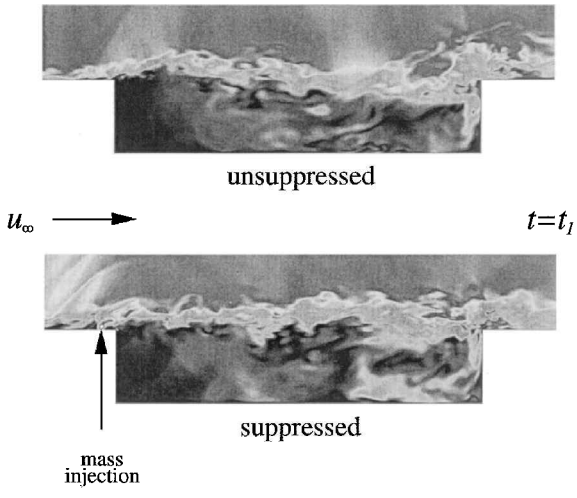

Fig. 12 Instantaneous Mach number contours at the midspan location for $t = t_1$.

overall effect is to reduce the level downstream and within the cavity. Profiles of turbulent kinetic energy are shown in Fig. 9, where the reduction is obvious, particularly downstream ($x = 0.8$). These profiles may be compared to that of the initial state of the incoming boundary layer in Fig. 2. The reduction in turbulent kinetic energy for the suppressed case is accompanied by a similar reduction in the mean fluctuating pressure $(p'p')_m$, which is shown by the contours in Fig. 10. The decrease in magnitude is most noticeable at the rear bulkhead. Fluctuating pressure profiles indicated in Fig. 11 quantify the mitigating effect of suppression.

Instantaneous Flowfields

Features of the unsteady cavity flowfields are elucidated by a series of instantaneous contours of Mach number, spanwise component of vorticity, and pressure coefficient in Figs. 12–23. These planar representations were generated at the midspan location, for four discrete instants in time, t_1, t_2, t_3, and t_4. Dynamics of the cavity flowfield are dominated by large-scale vortical structures that form aft of the forward bulkhead and convect downstream. These structures evolve through a roll up of the unstable shear layer, which is created as the boundary layer leaves the surface ahead of the cavity at the forward lip. The time sequence t_1, t_2, t_3, t_4 represents one cycle of the vortex shedding period, divided into equally spaced increments. Unsuppressed and suppressed results were synchronized, so that at each time instant contours from both cases corresponded to the identical point within the vortex shedding cycle.

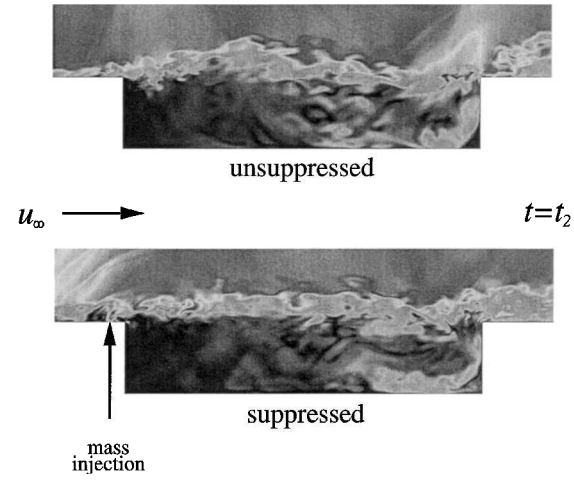

Fig. 13 Instantaneous Mach number contours at the midspan location for $t = t_2$.

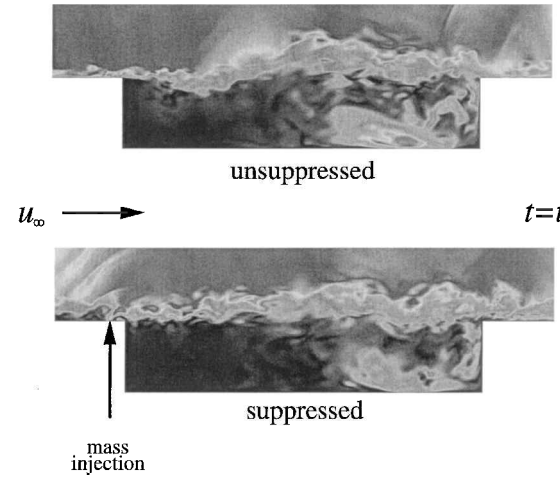

Fig. 14 Instantaneous Mach number contours at the midspan location for $t = t_3$.

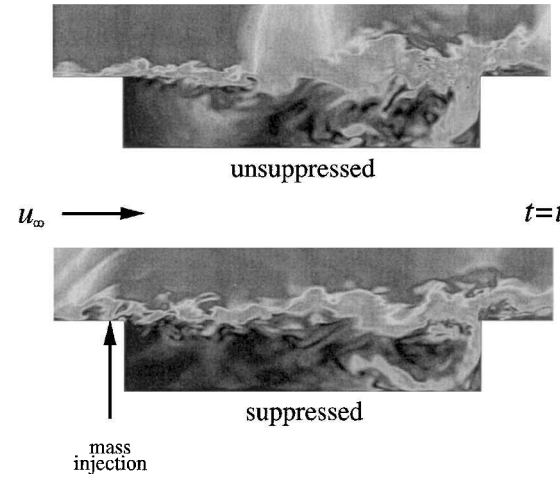

Fig. 15 Instantaneous Mach number contours at the midspan location for $t = t_4$.

At $t = t_1$ (Figs. 12, 16, and 20), one large vortical structure is forming in the upstream half of the cavity (Fig. 16), while another has been destroyed as it impacted the rear cavity lip. An oblique shock can be seen upstream of the forward lip for the unsuppressed case in the Mach number and pressure contours (Figs. 12 and 20). Strong acoustic waves produced by the forced injection are evident in the suppressed case, upstream of the forward lip. Within the vortex, fine-scale turbulence is apparent in the vorticity contours (Fig. 16).

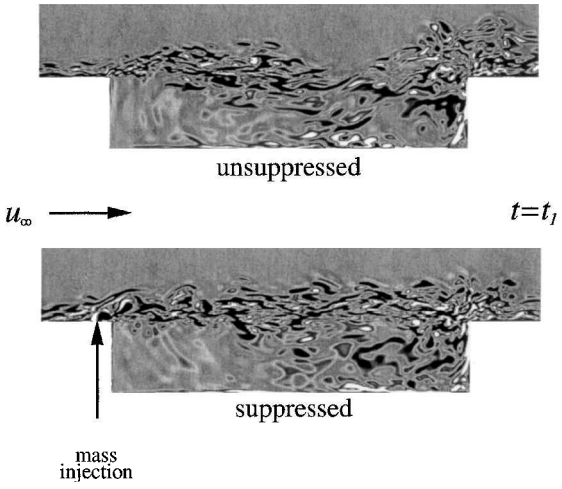

Fig. 16 Instantaneous spanwise vorticity contours at the midspan location for $t=t_1$.

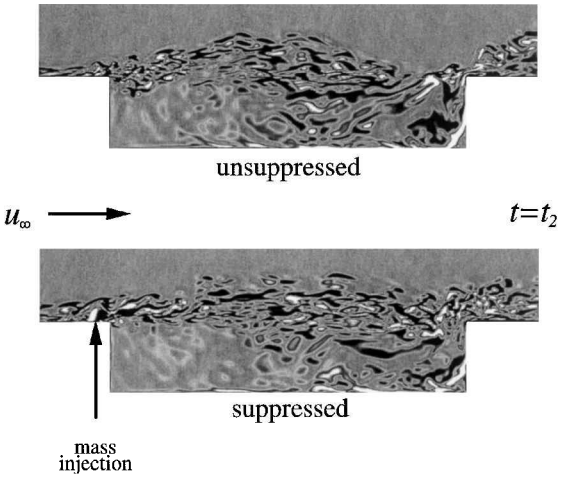

Fig. 17 Instantaneous spanwise vorticity contours at the midspan location for $t=t_2$.

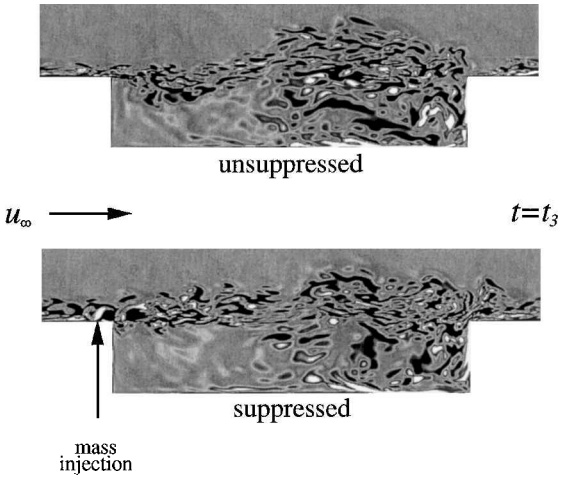

Fig. 18 Instantaneous spanwise vorticity contours at the midspan location for $t=t_3$.

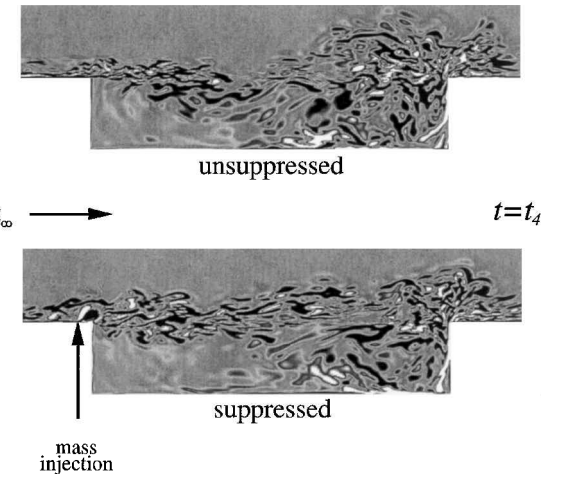

Fig. 19 Instantaneous spanwise vorticity contours at the midspan location for $t=t_4$.

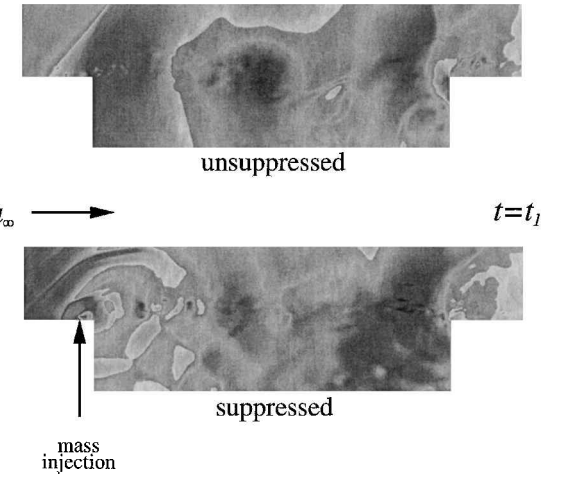

Fig. 20 Instantaneous pressure coefficient contours at the midspan location for $t=t_1$.

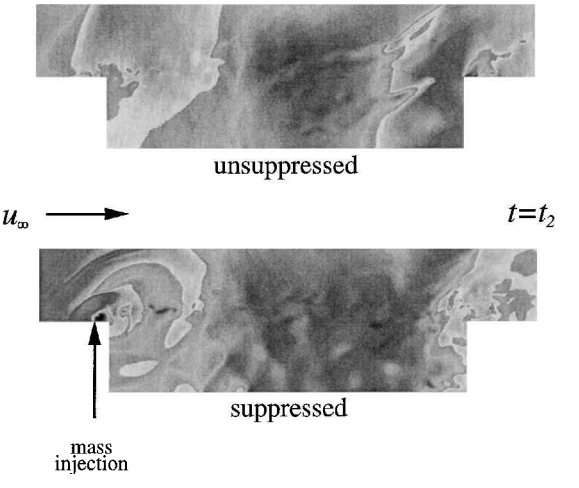

Fig. 21 Instantaneous pressure coefficient contours at the midspan location for $t=t_2$.

Fine-scale turbulence is also observed in the incoming boundary layer upstream of the forward lip. A low-pressure region (dark) within the vortex core can be observed in the contours of Fig. 20. The shear layer spanning the mouth of the cavity is most clearly illustrated by the Mach number contours in Fig. 12. Dark contours in Fig. 12 represent regions of slowly moving fluid. Figure 16 shows that the vortex of the suppressed case is weaker than its unsuppressed counterpart. This is because energy has been added to the shear layer through forced mass injection, and it is better able to withstand its natural tendency to roll up. In addition, the injection has disrupted the coherence of the shear layer.

Time frames at $t=t_2$ are presented in Figs. 13, 17, and 21. Here the vortex has moved farther downstream and now lies in the center of the cavity (Fig. 17). This has produced a large deflection of the shear layer in the unsuppressed case, resulting in the formation of an oblique shock wave just aft of the vortex. The shock wave is

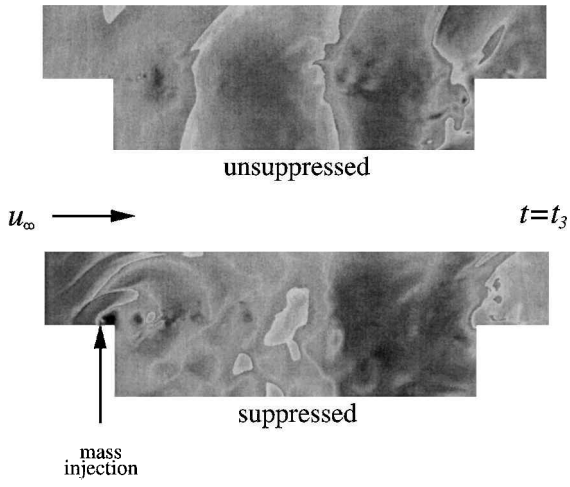

Fig. 22 Instantaneous pressure coefficient contours at the midspan location for $t = t_3$.

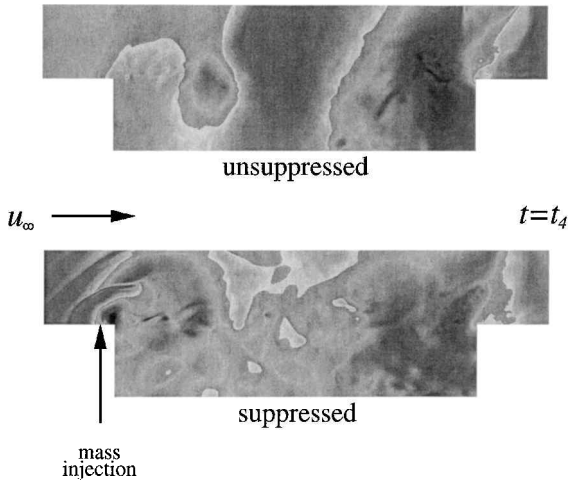

Fig. 23 Instantaneous pressure coefficient contours at the midspan location for $t = t_4$.

evident in both the Mach number and pressure contours (Figs. 13 and 21). Because the vortex is weaker and flatter in shape for the suppressed case, displacement of the shear layer and strength of the shock wave are reduced. We note that high-pressure areas associated with the oblique shock waves (light contours) and the low pressure of the vortex extend from the mouth to the floor of the cavity in the vertical direction (Fig. 21).

The vortex begins its impact upon the rear bulkhead at $t = t_3$ (Figs. 14, 18, and 22). Now, the shear layer at the upstream cavity lip has returned to an undeflected condition. An oblique shock is still located upstream of the vortex for the unsuppressed case, but is not present with suppression. Finally, at $t = t_4$ (Figs. 15, 19, and 23) the vortex fully impinges upon the rear bulkhead. The aft oblique shock has traveled downstream past the cavity lip, and the pressure at the rear bulkhead is low due to the vortex. The impingement is much less severe in the suppressed case, once again because the vortex is weaker and flatter. In Fig. 19, a new vortex can be seen forming downstream of the forward cavity lip, thus completing the shedding cycle.

An acoustic interference pattern can be discerned within the cavity in the instantaneous pressure contours for the suppressed case (Figs. 20–23). This is caused by pressure waves, emanating from the injection slot, which expand about the forward lip and propagate into the cavity. These waves eventually impact upon the floor of the cavity and are reflected from it. The reflected waves then interfere with new incoming waves to generate the observed pattern.

The three-dimensional cavity flowfield is shown in Fig. 24, which provides instantaneous total pressure coefficient contours at several

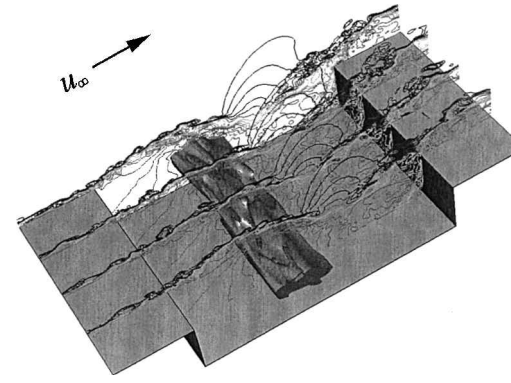

Fig. 24 Instantaneous total pressure coefficient contours and isosurface.

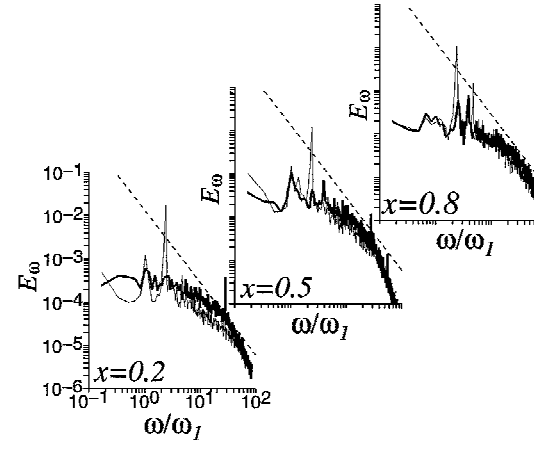

Fig. 25 Spanwise-averaged turbulent kinetic energy frequency spectra at $x = 0.2$, 0.5, and 0.8 and $y = 0.2\delta_0/l$: ——, unsuppressed; ▬▬, suppressed; and - - -, $-\frac{5}{3}$ slope.

spanwise stations, as well as an isosurface that illustrates the primary vortical structure. In this representation, the spanwise z direction has been stretched to view more easily details of the flowfield. Although many aspects of the flow have a dominant two-dimensional appearance, the fine-scale features are clearly three dimensional.

Statistical characteristics of the cavity acoustic resonance are illustrated by the turbulent kinetic energy frequency spectra shown in Fig. 25. To generate these spectra, instantaneous values of u, v, and w were recorded at three streamwise locations for $y = 0.2\delta_0/l$. This position is located within the turbulent shear layer over the mouth of the cavity. Turbulent kinetic energy frequency spectra were then constructed at each z location, and the results were averaged across the span. Figure 25 indicates two dominant modes, particularly in the unsuppressed case, and the frequency has been normalized by the first of these, ω_1. A reduction in amplitude of the dominant modes is found for all streamwise stations in the suppressed case. Addition of energy due to mass injection appears for $x = 0.2$ and 0.5 at $\omega/\omega_1 = 27.8$. Farther downstream at $x = 0.8$, the effect of this addition has diminished.

An alternate way of presenting the information of Fig. 25 appears in Fig. 26. In this case, the recorded values of u, v, and w were used to generate turbulent kinetic energy spanwise wave number spectra at each time step, and the results were then temporally averaged. Figure 26 shows that the energy is higher in the suppressed case at all streamwise locations, most noticeably at $x = 0.2$. Note that the locations represented in Fig. 26 lie within the shear layer where forced injection was initiated. Although the energy of the shear layer increased, peak amplitudes of the primary modes diminished.

Comparison with Experiments

Comparison with the experimental data of Refs. 27–30 is made in Figs. 27–31. This comparison consists of fluctuating pressure frequency spectra at discrete points located on the rear bulkhead

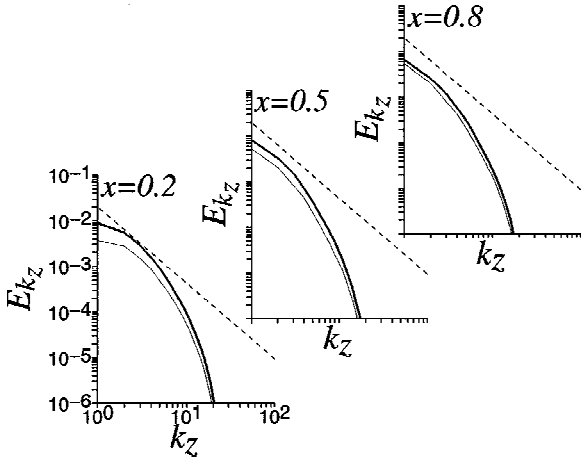

Fig. 26 Time-mean turbulent kinetic energy spanwise wave number spectra at $x = 0.2, 0.5$, and 0.8 and $y = 0.2\delta_0/l$: ——, unsuppressed; ▬, suppressed; and - - - -, $-\frac{5}{3}$ slope.

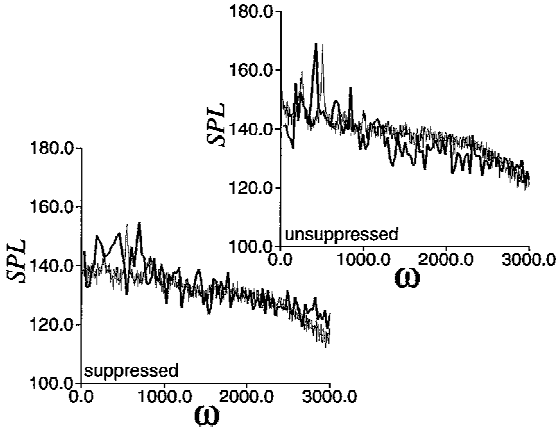

Fig. 27 Spanwise-averaged fluctuating pressure frequency spectra on the cavity rear bulkhead at $y = -0.04$, $x = 1.0$: ▬, LES and ——, experiment.

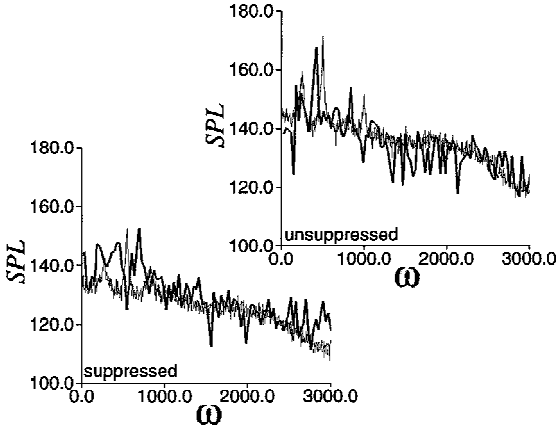

Fig. 28 Spanwise-averaged fluctuating pressure frequency spectra on the cavity rear bulkhead at $y = -0.08$, $x = 1.0$: ▬, LES and ——, experiment.

and the cavity floor. As was done for the turbulent kinetic energy, frequency spectra were constructed at every z location, and the results were then spanwise averaged. The amplitude of the fluctuating pressure is presented as sound pressure level (SPL) in decibels, and the frequency ω is given in hertz, as is customary for acoustic investigations, and is compatible with the experimental data. In terms of the nondimensional fluctuating pressure, the SPL was obtained as

$$\mathrm{SPL} = 20\log_{10}\left[\rho_\infty u_\infty^2 \sqrt{(p'p')_m}\Big/ q\right] \tag{21}$$

where $q = 2 \times 10^{-5}$ Pa.

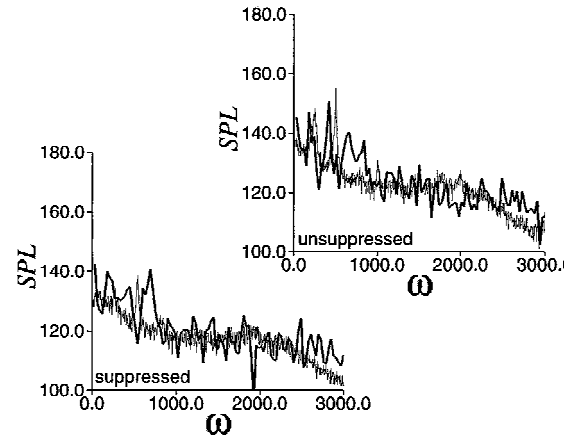

Fig. 29 Spanwise-averaged fluctuating pressure frequency spectra on the cavity floor at $x = 0.2$, $y = -0.2$: ▬, LES and ——, experiment.

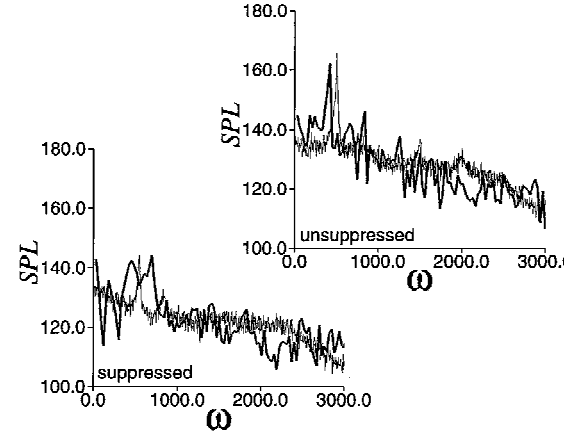

Fig. 30 Spanwise-averaged fluctuating pressure frequency spectra on the cavity floor at $x = 0.5$, $y = -0.2$: ▬, LES and ——, experiment.

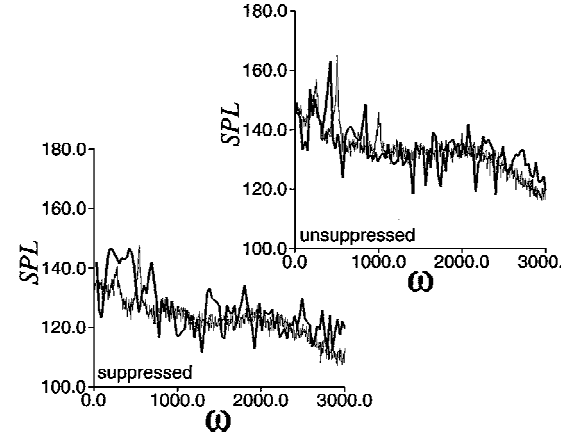

Fig. 31 Spanwise-averaged fluctuating pressure frequency spectra on the cavity floor at $x = 0.8$, $y = -0.2$: ▬, LES and ——, experiment.

The SPL on the rear bulkhead ($x = 1.0$) at $y = -0.04$ is seen in Fig. 27. This location is just below the aft lip of the cavity and experiences the highest pressures due to the oblique shock wave, which moves downstream preceding the vortex and passes over the lip. For the unsuppressed case, amplitudes of the computed SPL of the two dominant modes compare well to the experiment. The corresponding frequencies of these modes from the LES are somewhat smaller than those of the measurements. This is probably because the Reynolds number of the computations is considerably lower. Note that the experimental frequencies agree with the empirical relationship of Rossiter,[5] which is a high-Reynolds-number

correlation. When acoustic suppression is active, both the experiment and computation indicate a 15-dB reduction in the amplitude of the dominant mode.

SPLs on the rear bulkhead at $y = -0.08$ are shown in Fig. 28. The observed comparison is similar to that in Fig. 27. Figures 29–31 provide pressure levels at several streamwise locations along the floor of the cavity ($y = -0.2$). Amplitudes on the floor are not as high as those on the rear bulkhead. Reduction of the acoustic modes with suppression is apparent, and the LES compare favorably with the experiment.

The mass flux of forced injection for the suppressed case of the experimental configuration is approximately 145.6 kg/s $\cdot$ m^2. Smaller values of mass flux were also considered in the investigation, but were not effective in suppressing the acoustic resonant modes. In the LES, the time–mean mass flux was only 22% of the experimental value. When the full experimental value of mass flux was employed in the computation, massive separation occurred upstream of the injection slot. This resulted in a large displacement of the boundary layer and the formation of a near normal shock wave ahead of the displaced region. The normal shock wave then caused further separation of the boundary layer, and it began to travel upstream. Eventually the shock reached the upstream boundary, and the computation was terminated. The reason for this physical behavior was because the Reynolds number ($Re_{\delta 0}$) of the computed flow was an order of magnitude lower than that of the experiment (Table 1). Therefore, the boundary layer contained less energy and was not able to withstand the disruption of strong mass injection.

The second mode of the frequency spectra found in Figs. 25 and 27–31, which occurs at approximately 420 Hz for the LES, correlates with the shedding frequency of the vortical structure. Because an oblique shock wave is formed ahead of each vortex as it is shed, the second mode also corresponds the frequency with which the shock impinges upon the rear bulkhead. In addition, however, there is a system of unsteady pressure waves that characterize the acoustic resonance of the cavity. As each vortex forms, there eventually arises a pressure wave immediately beneath the vortex core, which travels downstream at about the convective speed of the vortex. When this wave impacts the aft bulkhead, it is reflected from the wall and then travels upstream. This reflected wave can be observed in Fig. 20 at the floor of the cavity just upstream of the aft bulkhead. As the wave travels upstream, it eventually passes another downstream moving wave beneath the next vortex that has formed. Eventually, the upstream moving wave impacts the forward bulkhead and is reflected as a downstream moving wave. By this time, yet another new vortex has already begun to form downstream of the forward lip. The newly reflected wave then catches up with the vortex and is synchronized with its downstream travel. Because this entire cycle corresponds to the shedding of two vortices, its frequency is one-half that of the second mode and, thus, represents the first mode seen in the spectra. This description, based on our observations, is consistent with those originally given by Rossiter[4,5] and Heller and Bliss,[9,10] but differs in some specific details.

Summary

LES were performed for the Mach 1.19 flow past a rectangular cavity with a length-to-depth ratio of 5:1. Spatial derivatives were represented by a fourth-order compact finite difference scheme that was used in conjunction with a sixth-order nondispersive filter. The Smagorinsky dynamic subgrid-scale model was incorporated in the simulations to account for spatially underresolved stresses. Fine-scale turbulent structures of the incoming boundary layer were provided by a separate direct simulation.

The computations were carried out on a mesh system consisting of 2.06×10^7 grid points, which were distributed over 254 processors of a parallel computing platform. Active flow control was applied through pulsed mass injection at a very high frequency (5000 Hz). Features of the turbulent flowfields were examined, and comparisons were made between the unsuppressed and suppressed cases. It was found that acoustic suppression resulted from the addition of energy to the shear layer flowing over the cavity. This addition altered characteristics of the vortices forming the shear layer and decreased the amplitude of shear layer excursions in the vertical direction. In addition, the acoustic interference pattern, set up within the cavity due to forced injection, helped to disrupt the natural wave system that occurs at resonance.

Comparisons were also made with available experimental data that were collected at a higher Reynolds number. Computed SPLs on the cavity floor and rear bulkhead agreed well with experimental data in both the unsuppressed and suppressed cases. These results were encouraging, especially considering that the Reynolds number of the simulations and the injected mass flow rate were lower than those of the experiment. It evidences the utility of LES for exploring flow control strategies for acoustic suppression of cavity resonance, as well as for other applications.

Acknowledgments

The work presented here was sponsored by the U.S. Air Force Office of Scientific Research under Task 2304N402 and was monitored by W. Hilbun and T. Beutner. Computational resources were supported in part by a grant of supercomputer time from the U.S. Department of Defense Major Shared Resource Centers at Stennis Space Center, Mississippi and Wright–Patterson Air Force Base, Ohio. The authors are grateful to M. J. Stanek for assistance in disseminating experimental data and for a number of helpful discussions.

References

[1]Krishnamurty, K., "Acoustic Radiation from Two-Dimensional Rectangular Cutouts in Aerodynamic Surfaces," NACA TN-3487, Aug. 1955.

[2]Charwat, A. F., Roos, J. N., Dewey, F. C., Jr., and Hitz, J. A., "An Investigation of Separated Flows—Part I: The Pressure Field," *Journal of the Aerospace Sciences*, Vol. 28, No. 6, 1961, pp. 457–470.

[3]Charwat, A. F., Dewey, C. F., Jr., and Roos, J. N., "An Investigation of Separated Flows—Part II: Flow in the Cavity and Heat Transfer," *Journal of the Aerospace Sciences*, Vol. 28, No. 7, 1961, pp. 513–527.

[4]Rossiter, J. E., and Kurn, A. G., "Wind Tunnel Measurements of the Unsteady Pressures In and Behind a Bomb Bay (Camberra)," CP 728, Ministry of Aviation, Aeronautical Research Council, London, Oct. 1962.

[5]Rossiter, J. E., "Wind Tunnel Measurements on the Flow Over Rectangular Cavities at Subsonic and Transonic Speeds," Ministry of Aviation, Repts. and Memoranda 3438, Aeronautical Research Council, London, Oct. 1964.

[6]East, L. F., "Aerodynamically Induced Resonance in Rectangular Cavities," *Journal of Sound and Vibration*, Vol. 3, May 1966, pp. 227–287.

[7]Heller, H., Holmes, G., and Covert, E., "Flow Induced Pressure Oscillations in Shallow Cavities," U.S. Air Force Flight Dynamics Lab., AFFDL-TR-70-140, Wright–Patterson AFB, OH, Dec. 1970.

[8]Bilanin, A. J., and Covert, E. E., "Estimation of Possible Excitation Frequencies for Shallow Rectangular Cavities," *AIAA Journal*, Vol. 11, No. 3, 1973, pp. 347–351.

[9]Heller, H., and Bliss, D., "Aerodynamically Induced Pressure Oscillations in Cavities: Physical Mechanisms and Suppression Concepts," U.S. Air Force Flight Dynamics Lab., AFFDL-TR-133, Wright–Patterson AFB, OH, Feb. 1975.

[10]Heller, H. H., and Bliss, D., "The Physical Mechanism of Flow-Induced Pressure Fluctuations in Cavities and Concepts for their Suppression," AIAA Paper 75-491, March 1975.

[11]Clark, R. L., "Weapons Bay Turbulence Reduction Techniques," U.S. Air Force Flight Dynamics Lab., AFFDL-TM-75-147, Wright–Patterson AFB, OH, Dec. 1975.

[12]Clark, R. L., Kaufman, L. G., II, and Maciulaitis, A., "Aero-Acoustic Measurements for Mach 0.6-3.0 Flows Past Rectangular Cavities," AIAA Paper 80-0036, Jan. 1980.

[13]Kaufman, L. G., II, Maciulaitis, A., and Clark, R. L., "Mach 0.6 to 3.0 Flows over Rectangular Cavities," U.S. Air Force Wright Aeronautical Labs., AFWAL-TR-82-3112, Wright–Patterson AFB, OH, May 1983.

[14]Stallings, R. L., and Wilcox, F. J., "Experimental Cavity Pressure Distributions at Supersonic Speeds," NASA-TP-2683, June 1987.

[15]Rizzetta, D. P., "Numerical Solution of Supersonic Flow over a Three-Dimensional Cavity," *AIAA Journal*, Vol. 26, No. 7, 1988, pp. 799–807.

[16]Shang, J. S., and Hankey, W. L., Jr., "Numerical Solution for Supersonic Turbulent Flow over a Compression Ramp," *AIAA Journal*, Vol. 13, No. 10, 1975, pp. 1368–1374.

[17]Kim, I., and Chokani, N., "Navier–Stokes Study of Supersonic Cavity Flowfield with Passive Control," *Journal of Aircraft*, Vol. 29, No. 2, 1992, pp. 217–223.

[18]Shih, S. H., Hamed, A., and Yeuan, J. J., "Unsteady Supersonic Cavity Flow Simulations Using Coupled κ–ϵ and Navier–Stokes Equations," *AIAA Journal*, Vol. 32, No. 10, 1994, pp. 2015–2021.

[19]Zhang, X., "Compressible Cavity Flow Oscillations Due to Shear Layer Instabilities and Pressure Feedback," *AIAA Journal*, Vol. 33, No. 8, Aug. 1995, pp. 1404–1411.

[20]Tam, C.-J., Orkwis, P. D., and Disimile, P. J., "Algebraic Turbulence Model Simulations of Supersonic Open-Cavity Flow Physics," *AIAA Journal*, Vol. 34, No. 11, 1996, pp. 2255–2260.

[21]Suhs, N. E., "Computations of Three-Dimensional Cavity Flow at Subsonic and Supersonic Mach Numbers," AIAA Paper 87-1208, June 1987.

[22]Baysal, O., Srinivasan, S., and Stallings, R. L., "Unsteady Viscous Calculations of Supersonic Flow Past Deep and Shallow Three-Dimensional Cavities," AIAA Paper 88-0101, Jan. 1988.

[23]Lillberg, E., and Fureby, C., "Large Eddy Simulation of Supersonic Cavity Flow," AIAA Paper 2000-2411, June 2000.

[24]Arunajatesan, S., Shipman, J. D., and Sinha, N., "Hybrid RANS–LES Simulation of Cavity Flow Fields with Control," AIAA Paper 2002-1130, Jan. 2002.

[25]Shaw, L., "Active Control for Cavity Acoustics," AIAA Paper 98-2347, June 1998.

[26]McGrath, S. F., and Shaw, L. L., "Active Control of Shallow Cavity Acoustic Resonance," AIAA Paper 96-1949, June 1996.

[27]Stanek, M. J., Raman, G., Kibens, V., Ross, J. A., Odedra, J., and Peto, J. W., "Control of Cavity Resonance Through Very High Frequency Forcing," AIAA Paper 2000-1905, June 2000.

[28]Ross, J. A., Peto, J. W., and Odedra, J., "Active Control of Cavity Resonance—Investigation of Acoustic Suppression Methods," Defence Evaluation Research Agency, Rept. WAIS 257, Bedford, England, U.K., Nov. 1999.

[29]Raman, G., and Kibens, V., "High Frequency Excitation Cavity Experiments," The Boeing Co., Rept. 00P0064, St. Louis, MO, April 2000.

[30]Odedra, J., Peto, J. W., and Ross, J. A., "Active Control of Cavity Resonance—Investigation of Acoustic Suppression Methods—Phase 2," Defence Evaluation Research Agency Report WAIS 260, Bedford, England, U.K., June 2001.

[31]Rizzetta, D. P., and Visbal, M. R., "Large-Eddy Simulation of Supersonic Cavity Flowfields Including Flow Control," AIAA Paper 2002-2853, June 2002.

[32]Rizzetta, D. P., Visbal, M. R., and Gaitonde, D. V., "Large-Eddy Simulation of Supersonic Compression-Ramp Flow by a High-Order Method," *AIAA Journal*, Vol. 39, No. 12, 2001, pp. 2283–2292.

[33]Germano, M., Piomelli, U., Moin, P., and Cabot, W. H., "A Dynamic Subgrid-Scale Eddy Viscosity Model," *Physics of Fluids A*, Vol. 3, No. 7, 1991, pp. 1760–1765.

[34]Yoshizawa, A., "Statistical Theory for Compressible Turbulent Shear Flows, with the Application to Subgrid Modeling," *Physics of Fluids*, Vol. 29, No. 7, 1986, pp. 2152–2164.

[35]Moin, P., Squires, W., Cabot, W., and Lee, S., "A Dynamic Subgrid-Scale Model for Compressible Turbulence and Scalar Transport," *Physics of Fluids A*, Vol. 3, No. 11, 1991, pp. 2746–2757.

[36]Beam, R., and Warming, R., "An Implicit Factored Scheme for the Compressible Navier–Stokes Equations," *AIAA Journal*, Vol. 16, No. 4, 1978, pp. 393–402.

[37]Gordnier, R. E., and Visbal, M. R., "Numerical Simulation of Delta-Wing Roll," AIAA Paper 93-0554, Jan. 1993.

[38]Jameson, A., Schmidt, W., and Turkel, E., "Numerical Solutions of the Euler Equations by Finite Volume Methods Using Runge–Kutta Time Stepping Schemes," AIAA Paper 81-1259, June 1981.

[39]Pulliam, T. H., and Chaussee, D. S., "A Diagonal Form of an Implicit Approximate-Factorization Algorithm," *Journal of Computational Physics*, Vol. 39, No. 2, 1981, pp. 347–363.

[40]Lele, S. A., "Compact Finite Difference Schemes with Spectral-like Resolution," *Journal of Computational Physics*, Vol. 103, No. 1, 1992, pp. 16–42.

[41]Visbal, M. R., and Gaitonde, D. V., "High-Order-Accurate Methods for Complex Unsteady Subsonic Flows," *AIAA Journal*, Vol. 37, No. 10, 1999, pp. 1231–1239.

[42]Gaitonde, D., Shang, J. S., and Young, J. L., "Practical Aspects of High-Order Accurate Finite-Volume Schemes for Electromagnetics," AIAA Paper 97-0363, Jan. 1997.

[43]Gaitonde, D., and Visbal, M. R., "High-Order Schemes for Navier–Stokes Equations: Algorithm and Implementation into FDL3DI," U.S. Air Force Research Lab., AFRL-VA-WP-TR-1998-3060, Wright–Patterson AFB, OH, Aug. 1998.

[44]Gordnier, R. E., and Visbal, M. R., "Numerical Simulation of Delta-Wing Roll," *Aerospace Science and Technology*, Vol. 2, No. 6, 1998, pp. 347–357.

[45]Gordnier, R. E., "Computation of Delta-Wing Roll Maneuvers," *Journal of Aircraft*, Vol. 32, No. 3, 1995, pp. 486–492.

[46]Visbal, M. R., "Computational Study of Vortex Breakdown on a Pitching Delta Wing," AIAA Paper 93-2974, July 1993.

[47]Visbal, M. R., "Onset of Vortex Breakdown Above a Pitching Delta Wing," *AIAA Journal*, Vol. 32, No. 8, 1994, pp. 1568–1575.

[48]Visbal, M., Gaitonde, D., and Gogineni, S., "Direct Numerical Simulation of a Forced Transitional Plane Wall Jet," AIAA Paper 98-2643, June 1998.

[49]Rizzetta, D. P., Visbal, M. R., and Stanek, M. J., "Numerical Investigation of Synthetic-Jet Flowfields," *AIAA Journal*, Vol. 37, No. 8, 1999, pp. 919–927.

[50]Rizzetta, D. P., Visbal, M. R., and Blaisdell, G. A., "Application of a High-Order Compact Difference Scheme to Large-Eddy and Direct Numerical Simulation," AIAA Paper 99-3714, June 1999.

[51]Rizzetta, D. P., and Visbal, M. R., "Application of Large-Eddy Simulation to Supersonic Compression Ramps," *AIAA Journal*, Vol. 40, No. 8, 2002, pp. 1574–1581.

[52]Adams, N. A., "Direct Simulation of the Turbulent Boundary Layer along a Compression Ramp at $M = 3$ and $Re_\theta = 1685$," *Journal of Fluid Mechanics*, Vol. 420, Oct. 2000, pp. 47–83.

[53]Sinha, N., Arunajatesan, S., Shipman, J., and Seiner, J. M., "High Fidelity Simulation and Measurements of Aircraft Weapons Bay Dynamics," AIAA Paper 2001-2125, May 2001.

[54]Suhs, N. E., Rogers, S. E., and Dietz, W. E., "PEGASUS 5: An Automated Pre-Processor for Overset-Grid CFD," AIAA Paper 2002-3186, June 2002.

[55]Message Passing Interface Forum, "MPI: A Message-Passing Interface Standard," Computer Science Dept., TR CS-94-230, Univ. of Tennessee, Knoxville, TN, April 1994.

M. Sichel
Associate Editor